Biomedical Optics EXPRESS

Measuring membrane association and protein diffusion within membranes with supercritical angle fluorescence microscopy

Yuanqing Ma,[1,2] Aleš Benda,[3,4] Philip R. Nicovich,[1,2] and Katharina Gaus[1,2,*]

[1]*EMBL Australia Node in Single Molecule Science, School of Medical Sciences, University of New South Wales, Sydney 2052 Australia*
[2]*ARC Center of Excellence in Advanced Molecular Imaging, University of New South Wales, Sydney 2052 Australia*
[3]*Biomedical Imaging Facility, Lowy Cancer Research Center, University of New South Wales, High Street, Kensington, Sydney, NSW, 2052, Australia*
[4]*IMCF at BIOCEV, Faculty of Science, Charles University in Prague, Czech Republic*
[*] *k.gaus@unsw.edu.au*

Abstract: Supercritical angle fluorescence (SAF) detection combines the axial discrimination and exquisite signal-to-noise ratio of total internal reflection fluorescence (TIRF) with the lateral discrimination and convenience of confocal excitation. This combination makes SAF ideal for fluorescence correlation spectroscopy (FCS) on membranes and other structures in close proximity to the coverslip. Here we report a straightforward modification of a commercial microscope to implement SAF FCS and demonstrate in both model supported lipid bilayers and cellular systems that this approach shows an increase in signal from membrane-bound fluorophores relative to fluorophores in solution, benchmarked against line-scanning FCS. SAF FCS allowed us to demonstrate that activation of the T cell receptor resulted in the recruitment of the kinase Lck to the plasma membrane as well as a reduction in Lck mobility within the membrane.

OCIS codes: (110.2945) Illumination design; (110.2970) Image detection systems; (300.6280) Spectroscopy, fluorescence and luminescence.

References and links

1. D. Toomre and D. J. Manstein, "Lighting up the cell surface with evanescent wave microscopy," Trends Cell Biol. **11**(7), 298–303 (2001).
2. T. Ruckstuhl and D. Verdes, "Supercritical angle fluorescence (SAF) microscopy," Opt. Express **12**(18), 4246–4254 (2004).
3. T. Ruckstuhl, D. Verdes, C. M. Winterflood, and S. Seeger, "Simultaneous near-field and far-field fluorescence microscopy of single molecules," Opt. Express **19**(7), 6836–6844 (2011).
4. E. Fort and S. Grésillon, "Surface enhanced fluorescence," J. Phys. D Appl. Phys. **41**(1), 013001 (2008).
5. J. Deschamps, M. Mund, and J. Ries, "3D superresolution microscopy by supercritical angle detection," Opt. Express **22**(23), 29081–29091 (2014).
6. C. M. Winterflood, T. Ruckstuhl, N. P. Reynolds, and S. Seeger, "Tackling sample-related artifacts in membrane FCS using parallel SAF and UAF detection," ChemPhysChem **13**(16), 3655–3660 (2012).
7. T. Barroca, K. Balaa, J. Delahaye, S. Lévêque-Fort, and E. Fort, "Full-field supercritical angle fluorescence microscopy for live cell imaging," Opt. Lett. **36**(16), 3051–3053 (2011).
8. J. Ries, T. Ruckstuhl, D. Verdes, and P. Schwille, "Supercritical angle fluorescence correlation spectroscopy," Biophys. J. **94**(1), 221–229 (2008).
9. N. L. Thompson and B. L. Steele, "Total internal reflection with fluorescence correlation spectroscopy," Nat. Protoc. **2**(4), 878–890 (2007).
10. J. Ries, E. P. Petrov, and P. Schwille, "Total Internal Reflection Fluorescence Correlation Spectroscopy: Effects of Lateral Diffusion And Surface-Generated Fluorescence," Biophys. J. **95**(1), 390–399 (2008).
11. M. Lever, P. K. Maini, P. A. van der Merwe, and O. Dushek, "Phenotypic models of T cell activation," Nat. Rev. Immunol. **14**(9), 619–629 (2014).

#255838 Received 21 Dec 2015; revised 16 Mar 2016; accepted 17 Mar 2016; published 29 Mar 2016

12. C. Walker, F. Bettens, and W. J. Pichler, "T cell activation by cross-linking anti-CD3 antibodies with second anti-T cell antibodies: dual antibody cross-linking mimics physical monocyte interaction," Eur. J. Immunol. **17**(11), 1611–1618 (1987).
13. J. Rossy, D. M. Owen, D. J. Williamson, Z. Yang, and K. Gaus, "Conformational states of the kinase Lck regulate clustering in early T cell signaling," Nat. Immunol. **14**(1), 82–89 (2012).
14. K. Nika, C. Soldani, M. Salek, W. Paster, A. Gray, R. Etzensperger, L. Fugger, P. Polzella, V. Cerundolo, O. Dushek, T. Höfer, A. Viola, and O. Acuto, "Constitutively Active Lck kinase in T Cells Drives Antigen Receptor Signal Transduction," Immunity **32**(6), 766–777 (2010).
15. H. Ike, A. Kosugi, A. Kato, R. Iino, H. Hirano, T. Fujiwara, K. Ritchie, and A. Kusumi, "Mechanism of Lck recruitment to the T-cell receptor cluster as studied by single-molecule-fluorescence video imaging," ChemPhysChem **4**(6), 620–626 (2003).
16. L. Zimmermann, W. Paster, J. Weghuber, P. Eckerstorfer, H. Stockinger, and G. J. Schütz, "Direct Observation and Quantitative Analysis of Lck Exchange Between Plasma Membrane and Cytosol in Living T Cells," J. Biol. Chem. **285**(9), 6063–6070 (2010).
17. N. Bourg, C. Mayet, G. Dupuis, T. Barroca, P. Bon, S. Lécart, E. Fort, and S. L. Fort, "Direct optical nanoscopy with axially localized detection," Nat. Photonics **9**(9), 587–593 (2015).
18. A. Benda, Y. Ma, and K. Gaus, "Self-calibrated line-scan STED-FCS to quantify lipid dynamics in model and cell membranes," Biophys. J. **108**(3), 596–609 (2015).
19. J. Riedl, A. H. Crevenna, K. Kessenbrock, J. H. Yu, D. Neukirchen, M. Bista, F. Bradke, D. Jenne, T. A. Holak, Z. Werb, M. Sixt, and R. Wedlich-Soldner, "Lifeact: a versatile marker to visualize F-actin," Nat. Methods **5**(7), 605–607 (2008).
20. A. Benda, M. Beneš, V. Mareček, A. Lhotský, W. T. Hermens, and M. Hof, "How To Determine Diffusion Coefficients in Planar Phospholipid Systems by Confocal Fluorescence Correlation Spectroscopy," Langmuir **19**(10), 4120–4126 (2003).
21. F. G. Gervais and A. Veillette, "The unique amino-terminal domain of p56lck regulates interactions with tyrosine protein phosphatases in T lymphocytes," Mol. Cell. Biol. **15**(5), 2393–2401 (1995).
22. U. Mets and R. Rigler, "Submillisecond detection of single rhodamine molecules in water," J. Fluoresc. **4**(3), 259–264 (1994).
23. J. Ries, S. Chiantia, and P. Schwille, "Accurate Determination of Membrane Dynamics with Line-Scan FCS," Biophys. J. **96**(5), 1999–2008 (2009).
24. E. Conibear and N. G. Davis, "Palmitoylation and depalmitoylation dynamics at a glance," J. Cell Sci. **123**(23), 4007–4010 (2010).
25. A. D. Douglass and R. D. Vale, "Single-molecule microscopy reveals plasma membrane microdomains created by protein-protein networks that exclude or trap signaling molecules in T cells," Cell **121**(6), 937–950 (2005).

1. Introduction

When incident light hits an interface between a material of high index of refraction and one of lower index at an angle above the critical angle, defined as $\sin^{-1}\left(n_1/n_2\right)$ where n_1 and n_2 are the refractive indices of the media at either side of the interface, the light is totally internally reflected within the higher index material. An evanescent field is created in the lower index material, a phenomenon exploited by total internal reflection fluorescence (TIRF) imaging. In this modality, only those fluorophores located close to the interface (< 200 nm for glass/water and visible wavelengths) are excited by the evanescent field. The emission is collected by an objective and focused onto a camera, yielding a convenient means to achieve a high signal-to-noise ratio (SNR) images of fluorophores near the glass/water interface, such as those in bilayers or cell plasma membranes [1].

Supercritical angle fluorescence (SAF) microscopy is an alternative approach that allows for selective detection of molecules at the glass-water interface with high SNR [2]. It can be viewed as the converse of TIRF microscopy. In SAF microscopy, the sample excitation can be realized by either wide-field or point scanning configuration. However, only the emission of molecules close to the surface is detected. This is because the normally non-propagating near-field emission of the fluorophores close to the interface is converted into far-field transmitting fluorescence at the refractive index discontinuity of the interface. This signal propagates directly in the glass to all directions including super-critical angles (> critical angle) while emitters far from the surface (> ~200 nm) are primarily detected at under-critical angles due to the refraction at the water to glass interface, which lowers the emission angle [3]. These super-critical angle fluorescence signals, which can be up to 34% of the total

#255838 Received 21 Dec 2015; revised 16 Mar 2016; accepted 17 Mar 2016; published 29 Mar 2016

energy emitted, can be collected by a high numerical aperture (NA) objective or a special reflection-based collector [2, 4]. The super- and under-critical angle signals can be further separated based on their spatial position in the back focal plane of the emission collector, providing a convenient means to separate signals from emitters close and far from the interface, respectively.

SAF can either be implemented in a wide-field or scanning configuration [2, 3, 5–7]. The former employs a camera to capture an image; this approach often uses a circular mask at the back focal plane to block under-critical angle fluorescence, which causes diffraction and deteriorated lateral resolution in the SAF channel [5, 7]. The second option is a confocal-like scanning approach, in which a focused beam excites fluorophores at the sample near the glass/water interface and single point detectors (PMTs or SPADs) collect the SAF signal. Here, the sample is scanned, either by moving the laser beam or the sample, and the detection volume is defined by the overlap of the focused excitation beam and the axial range of the SAF detection. Contrary to confocal detection no pinhole is required. Although slower in image acquisition, the scanning SAF approach is simpler to implement, particularly for spectral, polarization and/or time resolved detection as commonly done in standard laser scanning confocal microscopes.

The restriction of the detection volume both in lateral and axial direction makes SAF ideal for fluorescence correlation spectroscopy (FCS) measurements [8]. Although FCS measurements under TIRF illumination have also been reported, the emission must be laterally restricted, for example, by placing a plate with a pinhole in the center of the emission path [9, 10]. The lateral confinement of TIRF FCS is thus limited to the size of the aperture rather than to a diffraction-limited spot that is more advantageous for FCS. Due to this set up, TIRF-FCS encounter problems with photobleaching as a large area of the sample is illuminated and the recovery of the photobleached area is slow and often insufficient since the fluorophores have to travel a large distance before they arrive at the central detection area. In contrast, photobleaching is not an issue in SAF as photobleached molecules can be quickly recovered from emitters in close proximity. This ability to monitor an axially- and laterally-confined region makes SAF FCS a promising technique particularly for quantifying dynamics of species of interest within cell membranes.

The T cell signaling pathway is a membrane-localized group of proteins of particular interest due to the ability of these proteins to transfer information, such as the presence of antigen molecules, across the cell membrane and induce changes at the cell interior and ultimately inciting an immune response [11]. Integral in this process is the tyrosine kinase Lck, responsible for phosphorylation of the T cell receptor (TCR) after stimulation, which can be achieved, for example, with activating anti-CD3 antibodies [12]. Since the TCR-CD3 complex resides in the plasma membrane, only membrane-associated Lck is thought to be able to initiate TCR signaling [13]. Additionally, given that the fraction of Lck in the enzymatically active state does not change upon TCR activation [14], it is likely that a change in spatial organization of Lck is responsible for the increase in TCR phosphorylation [13, 15]. Direct exchange of cytosolic Lck to the membrane of activated T cells has been previously observed [16], which could result in an increase the molecular density of membrane-associated Lck and potentially alter the dynamic equilibrium of TCR phosphorylation. In order to quantify this potential increased associate, we set out to measure the diffusion and membrane association of the Lck membrane anchor domain Lck10, as well as full-length Lck, in resting and activated T cells.

To date, SAF is not widely used in the biological community due to the lack of commercial SAF instruments, although a number SAF studies with custom-built microscopes have published [3, 6, 8, 17]. In this study, we demonstrate that SAF could be adapted to a commercial microscope system (PicoQuant Microtime 200) with straightforward hardware alterations. In our setup, both under-critical angle fluorescence and SAF emission could be acquired simultaneously with separate detectors. We show that SAF provides increased axial

#255838 Received 21 Dec 2015; revised 16 Mar 2016; accepted 17 Mar 2016; published 29 Mar 2016

resolution improving the quality of membrane imaging and membrane dynamics measurements with reduced influence from cytosolic fluorophores. We employ SAF FCS to investigate the diffusion and concentration of membrane-associated Lck molecules prior to and post TCR triggering, which suggests a translocation of Lck to the immune synapse upon T cell activation.

2. Materials and methods

2.1. Description of the SAF set-up

The custom-made SAF objective (from Dr Thomas Ruckstuhl [2], Fig. 1(a)) contains an aspheric lens centered along the optical axis with a 1.0 numerical aperture and 3 mm focal length. A collimated excitation laser is focused to a diffraction-limited spot by the aspheric lens and the emitted fluorescence is collected by two separate optical paths. The far field fluorescence emitted at under-critical angles relative to the optical axis is collected by the aspheric lens. The super-critical angle fluorescence emission is collected by a circular parabolic mirror. The angle of tilt and curvature of the parabolic mirror was designed so that the reflected SAF fluorescence was fully collimated regardless of the emitting angle. The fluorescence from both optical paths is collimated before reaching the back aperture of the objective. To avoid any bleed-through of UAF emission into SAF detection, an opaque ring mask was placed at the back aperture of the objective to block fluorescence emitted slightly below supercritical angle (Fig. 1(a)). Depending on the refractive index of the sample, a ring mask of varying width was used.

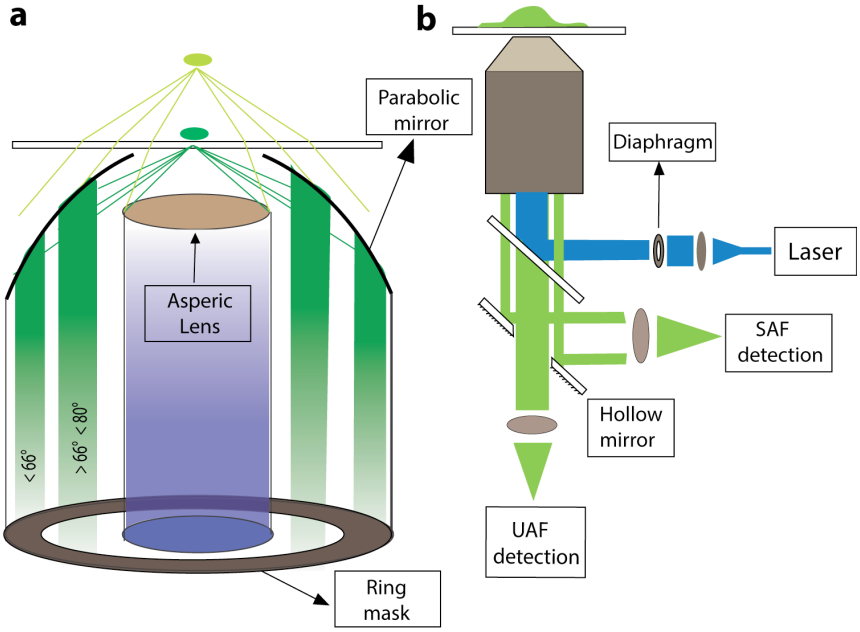

Fig. 1. Schematic setup of the SAF microscope. (**a**) The light path of the SAF objective. A collimated excitation laser (blue) is focused to a diffraction-limited point at by a central aspheric lens with f = 3 mm. Emission (green) at low angles (UAF) is collected by this same lens with higher-angle emission (SAF) collected by a confocal parabolic mirror. Intermediate angles of emission are blocked by an opaque ring mask in the back focal plane of the objective. (**b**) The collimated SAF and UAF emission beams are split by a mirror placed at the conjugate sample plane of the objective. In the mirror, a 3 mm x 4.5 mm elliptical hole was made to pass UAF and reflect SAF. Finally, the separated UAF and SAF fluorescence are each refocused onto the active area of the photodetectors.

#255838 Received 21 Dec 2015; revised 16 Mar 2016; accepted 17 Mar 2016; published 29 Mar 2016

The SAF objective was incorporated into a Microtime 200 (PicoQuant) system, which is based on an Olympus IX71 inverted microscope with a PI P-733.2CL XY objective scanner (Physik Instrumente). Excitation is provided by pulsed diode lasers (PicoQuant, P-C-470 LDH series, 470 nm, 0.4 mW at 40 MHz). Fluorescence emission is separated from excitation with a beamsplitter mirror (21001, CHROMA) with detection onto two SPAD photodetectors (PDM series, PicoQuant), each with a 100μm wide active area.

The incorporation of SAF objective into the Microtime 200 system requires two modifications to the light path. One is the insertion of a size adjustable diaphragm to the excitation light path after the optical fiber collimator to control the diameter of laser beam (Fig. 1(b)) to match the diameter of the aspheric lens (here 5.5 mm). Additionally a mirror is placed at the conjugate image plane in the emission light path to separate emission of UAF and SAF (Fig. 1(b)). Considering the mirror needed to be placed 45° relative to the light path, an elliptical hole of 3 mm x 4.5 mm in diameter was made. The position of the mirror is adjusted such that the UAF light passes through the hole, and the donut-shaped SAF signal is reflected. After the mirror, both UAF and SAF signals passed matched bandpass filters and are refocused onto the active area of the two separate detectors. The SPAD detector area used is 100 um in diameter. Given the Airy unit of 1.22*0.520/1.0 = 0.6344 um, and 10-times optical magnification along the light path, the detector area is 15.8 times larger than the Airy unit.

LS FCS was performed with a Lecia TCS SP5 confocal laser scanning microscope as previously described [18] using a 100x 1.4 NA oil-immersion objective coupled with a 150 μm pinhole. Laser excitation was provided by a 40 MHz pulsed white light laser with a central wavelength of 488 nm selected. The emitted photons were received by an external MPD detector (Picoquant) through the external light port of the Leica microscope. The timing of photon arrivals and photon counting was conducted by a TimeHarp 260 (PicoQuant) TCSPC board.

2.2. Cell culture, transfection, and imaging

COS-7 cells were cultured in Dulbecco's Modified Eagle's medium (DMEM) that was supplemented with 10% fetal bovine serum (FBS). Jurkat E6.1 cells were cultured in Roswell Park Memorial Institute medium (RPMI) supplemented with glutamine and 10% FBS. All cells were cultured in 37°C incubators with 5% CO_2. COS-7 cells were transfected with Lipofectamine LTX (Invitrogen) in glass-bottomed Fluorodish cell culture dishes (Coherent Scientific) 18 h prior to imaging. Jurkat cells were transfected by micro-electroporation (Invitrogen Neon) according to manufacturer's protocol. The culture medium was exchanged to phenol red-free medium prior to imaging. All cell lines were tested and confirmed to be *Mycoplasma* negative.

Cells were imaged under ambient conditions within 5 minutes of removal from the culture incubator. The FCS measurements were all conducted in cells of lower expression levels to ensure a sufficient contrast in fluorophore fluctuation.

2.3. Plasmid construction

DNA oligonucleotides were purchased from Sigma Aldrich Australia. The construct of Lifeact-Venus was constructed by integrating the Lifeact peptide [19] sequence to the N-terminus of the yellow fluorescent protein Venus and inserted into the mammalian expression vector pcDNA-3 (Addgene) using EcoRI and NotI restriction enzymes. Primer sequences used for the construction of Lifeact-YFP are Lifeact EcoRI FW: 5′- AAT GAA TTC ATG GGT GTC GCA GAT TTG ATC AAG AAA TTC GAA AGC ATC TCA AAG GAA GAA GGC GAT CCT CCA GTT GCT ACT GCG GAT CCA CCG GTC GCC ACC ATG GTG AGC AAG GGC GAG GAG CT –3′ and YFP NotI RV: 5′- AAT GCG GCC GCT TAC TTG TAC AGC TCG TCC ATG CCG AGA GT –3′. The construct of Lck10-EGFP was constructed by integrating the Lck10 motif to the N-terminus of EGFP and inserting into

#255838 Received 21 Dec 2015; revised 16 Mar 2016; accepted 17 Mar 2016; published 29 Mar 2016

pcDNA-3 at the EcoRI and NotI cutting sites. Primer sequence used for Lck10-GFP EcoRI FW: 5′- AAT GAA TTC ATG GGC TGT GTC TGC AGC TCA AAC CCT GAA GGA GGA GGA GGG GAT CCA AGT GCG ATT AAG CCA GAC ATG GTG AGC AAG GGC GAG GAG CT –3′ and GFP NotI RV: 5′- AAT GCG GCC GCT TTA CTT GTA CAG CTC GTC CAT GCC G –3′. The construct EGFP N1 was purchased from Clontech. *Phusion* DNA polymerase (New England BioLabs) was used for all PCR reactions. Plasmid sequences were confirmed by BigDye Terminator v3.1 Cycle Seuqencing (Life Technologies) at the Ramaciotti Center for Genomics at the University of New South Wales.

2.4. Preparation of supported lipid bilayer

Supported lipid bilayers were prepared from lipid mixtures of DOPC (1,2-dioleoyl-sn-glycero-3-phosphocholine, Avanti Polar Lipid) with DHPE 1,2-Dihexadecanoyl-sn-Glycero-3-Phosphoethanolamine (Thermo Fisher Scientific) with DHPE labelled with the flurophore Oregon Green 488 (DHPE-OG488). The lipid mixture was dissolved in chloroform, dried under nitrogen flow and stored under vacuum. The dried lipid film was rehydrated in 10 mM HEPES buffer containing 150 mM NaCl and 100 μM EDTA before sonicating using a tip sonicator (Sonifier 250, Branson) on ice until clear. The resulting liposome solution was filtered through a 0.22 μm syringe filter and applied to a 35 mm diameter glass bottom Fluorodish (World precision instruments). $CaCl_2$ (2mM final concentration) was added to the lipid mixture to initiate bilayer formation. Bilayers were washed 5 times with HEPES buffer prior to imaging. Where indicated, ATTO 488 (ATTO-TEC) was dissolved in water and used at the indicated concentration.

2.5. FCS correlation functions and 2-dimensional free diffusion models

The normalized auto-correlation $G(\tau)$ calculates the correlation of the intensity fluctuation $I(t)$ at a given time to the fluctuation at a later delayed time $I(t+\tau)$, given as:

$$G(\tau) = 1 + \frac{\langle \delta I(t) \delta I(t+\tau) \rangle}{\langle I(t)^2 \rangle} \tag{1}$$

the cross-correlation between different SAF and UAF channels is described as:

$$G(\tau)_{cross} = 1 + \frac{\langle \delta I_{SAF}(t) \delta I_{UAF}(t+\tau) \rangle}{\langle I_{SAF}(t) I_{UAF}(t) \rangle} \tag{2}$$

where $< >$ indicates intensity averaging over the acquisition time, δ is the intensity deviation from mean and τ the lag time.

When fluorophore diffusion is restricted to only two dimensions, as in the case of a typical lipid membrane, the spatial distribution of the detection volume can be given as a two-dimensional Gaussian function, and the resulting auto-correlation function is given as:

$$G(\tau) = \frac{1}{C\pi\omega_0^2} \left(1 + \frac{4\tau_D}{\omega_0^2} \right)^{-1} \tag{3}$$

where C is the number of fluorophores within the detection volume, ω_0 is the diameter of the detection volume beam waist, and τ_D is the diffusion time extracted from the correlation function. Here the diffusion coefficient, D, is determined by:

$$D = \frac{\omega_0^2}{4\tau_D} \tag{4}$$

In the case of two species diffusion model, the contribution to the overall correlation curve is additive and weighted by their individual amplitudes (A), which can be described as:

#255838 Received 21 Dec 2015; revised 16 Mar 2016; accepted 17 Mar 2016; published 29 Mar 2016

$$G = \frac{A_1^2 G_1 + A_2^2 G_2}{\left(A_1 + A_2\right)} \tag{5}$$

Given the dumbbell shape of the illumination profile, where the beam waist is narrowest at the focal point, the values for the diffusion time and particle number should similarly be at a minimum at the focal point. Deviating axially from this point increases the effective beam waist resulting in an increase both parameters. It has been demonstrated that the objective beam waist could be directly extracted by fitting the diffusion time τ_D or particle number PN to the parabolic function of z-scan FCS [20], as shown below:

$$\tau_D = \frac{\omega_0^2}{4D}\left(1 + \frac{\lambda^2 \Delta z^2}{\pi^2 n^2 \omega_0^2}\right) \tag{6}$$

$$PN = \pi c \omega_0^2 \left(1 + \frac{\lambda^2 \Delta z^2}{\pi^2 n^2 \omega_0^4}\right) \tag{7}$$

where λ is the excitation wavelength, Δz is the distance between objective focusing position and the focal plane of minimal beam waist, c is the concentration of fluorophores within the excitation volume and n is the refractive index of the medium.

The $T_{1/2}$ method is used for robust analysis of the average diffusion coefficient, where the auto-correlation function is poorly fitted by a one-species two-dimensional free diffusion model. In the $T_{1/2}$ method, the correlation curve is smoothed by taking the moving average of 60 adjacent data points. The diffusion time is defined as the lag time where the amplitude of the smoothed correlation curve drops to 50% of its initial value in the chosen time window of 200 μs to 1 s. The correlation value at 200 μs is defined as $G(0)$ for concentration analysis. The diffusion coefficient and concentration extracted by $T_{1/2}$ method is referred as effective diffusion coefficient and effective number of molecules per μm^2 or per μm^3 in current study.

The molecular brightness is defined as photon counts per second per molecule (cpsm). This is calculated by dividing the average photon counts per second of the intensity time trace by the number of molecules extracted by $T_{1/2}$ method.

3. Results and discussion

3.1. Characterization of SAF for membrane FCS measurements

Images of F-actin filaments in COS-7 cells (labeled by Lifeact-Venus) (Fig. 2(a), 2(b)) showed that the actin fiber patterns acquired in UAF and SAF were clearly different, indicating the difference in axial information contained in each channel. The SAF image had a sharp contrast of the fibers with a high SNR where only a thin layer of actin fibers close to the proximal cell surface was visible. In contrast, the UAF images resembled epifluorescence images where multiple overlaid layers of actin fibers were visible.

X-Z scans were performed with membrane-labeled cells in separate experiments. Here, live COS-7 cells were transfected with a GFP construct that contained the membrane localization motif of tyrosine kinase Lck [21] (Lck10-EGFP) such that GFP was localized at the plasma membrane. As expected, the images reveal that the UAF channel (Fig. 2(c)) captures fluorescence from a larger axial range, while the SAF channel only collected the fluorescence emitted from the cell membrane adjacent to the coverslip (Fig. 2(d)). The sharp contrast in vertical direction and the localized excitation in the lateral direction demonstrate the superiority of the SAF objective for selectively imaging samples close to the coverslip surface such as tagged proteins in membranes.

#255838 Received 21 Dec 2015; revised 16 Mar 2016; accepted 17 Mar 2016; published 29 Mar 2016

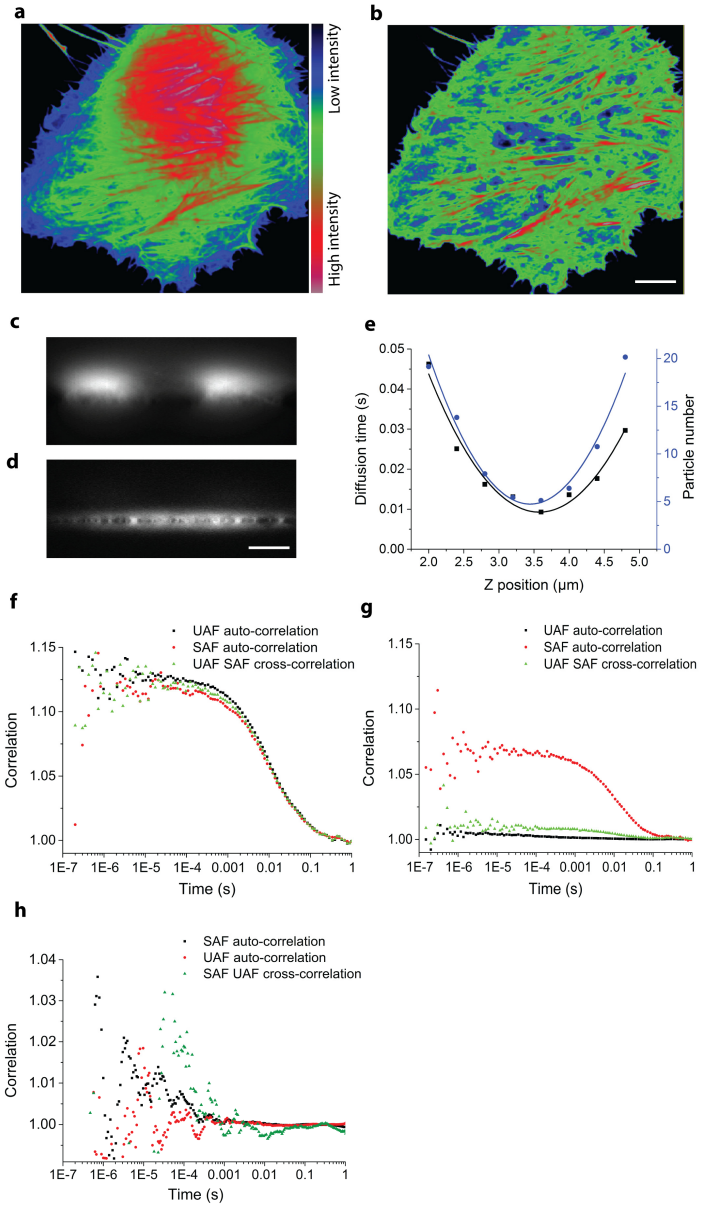

Fig. 2. SAF measurements in lipid bilayers. Representative UAF (**a**) and SAF (**b**) images of live COS-7 cells expressing Lifeact-Venus. The images are colored blue to red to indicate low to high pixel intensity. Scale bar = 5 μm. Data in **a** and **b** are representative of 5 cells. (**c, d**) x-z images of COS-7 cells expressing Lck10-EGFP recorded in the UAF (**c**) and SAF (**d**) channels. Scale bar = 3 μm (**e**) Quantification of diffusion time of DHPE-OG488 in a supported lipid bilayer (black, left axis) and SAF FCS beam waist (blue, right axis) as measured by z-scan SAF FCS. Measurements were taken at different focal positions 0.5 μm apart. Data (symbols) were fitted to a parabolic function (lines, Eqs. (6) and (7)) [20]. R^2 = 0.962 for diffusion time and R^2 = 0.970 for particle number, respectively) (**f**) SAF FCS, UAF FCS and cross-correlation of SAF and UAF of DHPE-OG488 (1 nM) in a supported lipid bilayer. (**g**) SAF FCS, UAF FCS and cross-correlation of SAF and UAF of ATTO 488 dye (100 nM) in solution above a supported lipid bilayer containing DHPE-OG488 (1 nM). (**h**) SAF FCS, UAF FCS and cross-correlation of SAF and UAF of ATTO 488 (100 nM) in solution. Data in **f**, **g**, and **h** is representative of 6 measurements.

#255838 Received 21 Dec 2015; revised 16 Mar 2016; accepted 17 Mar 2016; published 29 Mar 2016

To perform FCS with the SAF channel, we first characterized the diameter of the SAF excitation beam waist. This was done by measuring the diffusion of fluorescent lipids, namely Oregon Green 488 conjugated to 1,2-Dihexadecanoyl-*sn*-Glycero-3-Phosphoethanolamine (DHPE-OG488) in a supported lipid bilayer with z-scan FCS. In FCS, the molecular diffusion time and particle number are sensitive to the beam waist, ω_0, of the excitation laser. The SAF FCS beam was characterized using z-scan FCS. Here diffusion time and particle number for fluorescent DHPE-OG488 lipids within a supported lipid bilayer were measured while stepping the focal position at 0.5 μm intervals over the distance of 3.0 μm. Autocorrelation curves for signals obtained at each position were fit to a 1-species, two-dimensional diffusion model [8, 20]. When each parameter was plotted against the z-position (Fig. 2(e)), both term could be described by a parabolic function (Eqs. (6) and (7), respectively) [20]. Fitting returned the objective beam waist as 301 nm and 281 nm, respectively, for the two curves. Considering the NA of our objective is 1.0, the theoretical resolution is estimated as $1.22\lambda / 2NA$, or 286 nm for this system, agreeing well with the experimentally derived values.

Previous work [2] has shown that SAF detection volume in the z-direction is ~150 nm, suggesting that the detection volume of the SAF objective is ~0.01fL, or one order of magnitude smaller than a confocal detection volume [22]. This reduction in detection volume is beneficial for measuring samples that would be too concentrated for conventional FCS.

The overlap between excitation and collection volumes in the SAF system is confirmed by cross-correlating the SAF and UAF signals obtained with the objective focused on a DHPE-OG488-containing lipid bilayer. Given that the diffusion is restricted at two-dimensional lipid bilayers, if the SAF and UAF detection volumes (or, rather, the detection volumes of the aspheric lens excitation and collection and the parabolic mirror collection) truly overlap with each other the fluorescence fluctuations in the two channels will have originated from the same molecules as these molecules diffuse in and out of the detection volume. The autocorrelation signals seen in Fig. 2(f) (black and red dots) are nearly identical, demonstrating that the excitation volume within the lipid bilayer from the aspheric lens overlaps with both the collection volume of the aspheric lens (UAF signal) and the collection volume of the parabolic mirror (SAF signal). The overlapping cross-correlation signal confirms this overlap as this result requires that molecules transit between both the aspheric lens and parabolic mirror collection volumes simultaneously.

It was expected that the UAF detection volume would extended more deeply in the z-direction than that of the SAF, meaning the UAF channel would capture molecules in the solution above the lipid bilayer. To test this, ATTO 488 dye at a final concentration of 100 nM was added atop the Oregon-Green 488-containing lipid bilayer. In accordance with the strong z-discrimination, the SAF autocorrelation was minimally affected by the addition of soluble ATTO 488 solution as seen by the small decrease in amplitude of the SAF autocorrelation signal between Fig. 2(f) versus that in Fig. 2(g). On the other hand the UAF autocorrelation was vastly reduced due to the overwhelming contribution of the highly concentrated ATTO 488 signal (Fig. 2(g)). Under these conditions there was minimal cross-correlation between SAF and UAF. We also measured SAF and UAF FCS measurements with ATTO 488 in solution, which only resulted in weak autocorrelations under either SAF or UAF at fast correlations time of around 20 μs (Fig. 2(h)). This meant that with our set-up, free dye molecules in solution did not contribute to the correlation function in the time window of 200 μs to 1 s. Only correlations within this time window are considered in subsequent experiments. Together these measurements with supported lipid bilayers clearly demonstrated the z-discrimination of SAF and its ability to restrict measurements to areas immediately adjacent to the coverslip, which motivated us to apply SAF FCS to cellular membranes.

#255838 Received 21 Dec 2015; revised 16 Mar 2016; accepted 17 Mar 2016; published 29 Mar 2016

3.2. Comparison of SAF FCS with line-scanning FCS (LS FCS) for membrane diffusion analysis

One of the difficulties for membrane FCS measurements is that the molecule of interest may not be stably localized to the plasma membrane. There is often a fraction of the molecules in the cytoplasm, which diffuse at a much fast pace. In conventional confocal-based membrane FCS measurements the signal can be dominated by the cytosolic fraction, which skews the data and makes the extraction of diffusion parameters within the membrane complicated.

Here we investigated whether the SAF configuration could be used to reject the contribution of cytosolic molecules in FCS measurements of membrane-associated proteins in live cells. We chose to compare SAF FCS to line-scanning FCS (LS FCS) because of the advantages of LS FCS. Compared to traditional single-point FCS, LS FCS exhibits reduced photobleaching and enhanced statistical robustness due to spatial averaging over the scanning line. As a result LS FCS data tend to be less influenced by the heterogeneity of the membrane dynamics [23] and provide a benchmark which to compare the performance of SAF FCS in such biological systems.

We compared the diffusion coefficient of DHPE-OG488 in supported lipid bilayers by SAF FCS and LS FCS. Given that UAF can be acquired easily in parallel to SAF measurement, the UAF FCS was also included in the analysis. As seen in Fig. 3(a), the correlation curves in LS FCS, SAF FCS and UAF FCS could all be fit to a single species two-dimensional diffusion model Eq. (3). The amplitude of the correlation function decreased from LS FCS to SAF FCS and to UAF FCS, while the diffusion time was often shortest in LS FCS, followed by UAF and SAF. This is attributable to the smaller detection volume of the 100x NA1.4 oil-immersion objective used in LS FCS (measured to be 175 nm and 295 nm, for LS FCS and SAF FCS, respectively) and consequently smaller number and residence time of fluorescent particles seen in in these experiments.

The assessment of diffusion coefficient is not biased by the variation of objective beam waist between LS FCS and SAF FCS and provides a consistent measure to compare these two measurement modalities. For the same reason, the concentration was converted from particles per focal volume to number of molecules per μm^2. After compensating for the disparate beam waists, the FCS measurements show no difference in diffusion coefficient and number of molecules detected per μm^2 (Fig. 3(b), 3(c)). This strongly suggests that the parameters extracted were not biased by differences in instrumentation.

To demonstrate that SAF FCS is less influenced by the cytosolic fraction of the molecules, we measured the diffusion and concentration of Lck10-GFP in transfected COS-7 cells. Because the Lck10 motif interacts with plasma membrane *via* lipid modifications, namely myristoylation and palmitoylation, the protein anchor associates with the membrane in a reversible and dynamic manner [24]. Thus it is highly likely that there is always a cytosolic fraction of the GFP in the cell.

For SAF and UAF measurements, we set the focus on the plasma membrane by maximizing the coverslip-scattered light as captured by a CCD camera imaging at the primary dichroic mirror. For LS FCS, the focusing was achieved by maximizing the photon counts of the line scan. As with the supported lipid bilayer experiments, we first attempted to fit the resulting autocorrelation curves to a one-species, two-dimensional diffusion model. As can be seen in Fig. 3(d), a large portion of the autocorrelation obtained with LS FCS failed to fit to this model. The fit was significantly improved by a two-species two-dimensional diffusion model Eq. (5), Fig. 3(d). In contrast, the autocorrelation curves obtained with SAF FCS could still be well fit to the one-species model, while the use of a 2-species model further improved the fit. In order to facilitate comparison of the results from the LS FCS and SAF FCS measurements all the data were fitted to the two-species two-dimensional diffusion model.

The data suggest that the diffusion coefficients of the two Lck10-EGFP populations, presumably the membrane-bound and cytosolic fractions, were 1.09 ± 0.25 $\mu m^2/s$ (LS FCS)

#255838 Received 21 Dec 2015; revised 16 Mar 2016; accepted 17 Mar 2016; published 29 Mar 2016

and 0.96 ± 0.38 $\mu m^2/s$ (SAF FCS) for the membrane species and 39.76 ± 9.82 $\mu m^2/s$ (LS FCS) and 50.4 ± 32.5 $\mu m^2/s$ (SAF FCS) for the cytosolic species (Fig. 3(e)). These results are not significantly different between the two techniques (P = 0.35 and 0.31 for the membrane and cytosolic species, respectively). In order confirm that the fast diffusing species was cytosolic, we performed SAF FCS of cytosolic EGFP in COS-7 cells in a separate experiment (Fig. 3(f)). Indeed, the diffusion of cytosolic EGFP was collected by SAF objective in the time window (200 μs to 1s) we analyzed. The diffusion coefficient of the cytosolic EGFP was comparable to the fast diffusing component of EGFP in Fig. 3(e).

A difference is seen in the ratio of the amplitudes of the membrane-bound relative to the cytosolic components. Here the membrane-bound fraction amplitude was two-fold higher in SAF FCS than LS FCS (Fig. 3(g), $*P$ = 0.012). This suggests that the fluorescence fluctuations collected with the SAF objective were weighted towards the membrane-bound fraction of GFP molecules relative to those in LS FCS. This follows that the excitation efficiency decreases exponentially as the molecules move away from the coverslip surface in the SAF channel, enhancing the fluctuation signal of the coverslip-adjacent membrane-bound molecules over the distal cytosolic. In contrast the brightness of the membrane and cytosolic GFP molecules would be comparable in LS FCS so that the diffusion of the cytosolic fraction made a greater contribution to the overall intensity fluctuations versus what is observed in SAF FCS.

#255838 Received 21 Dec 2015; revised 16 Mar 2016; accepted 17 Mar 2016; published 29 Mar 2016

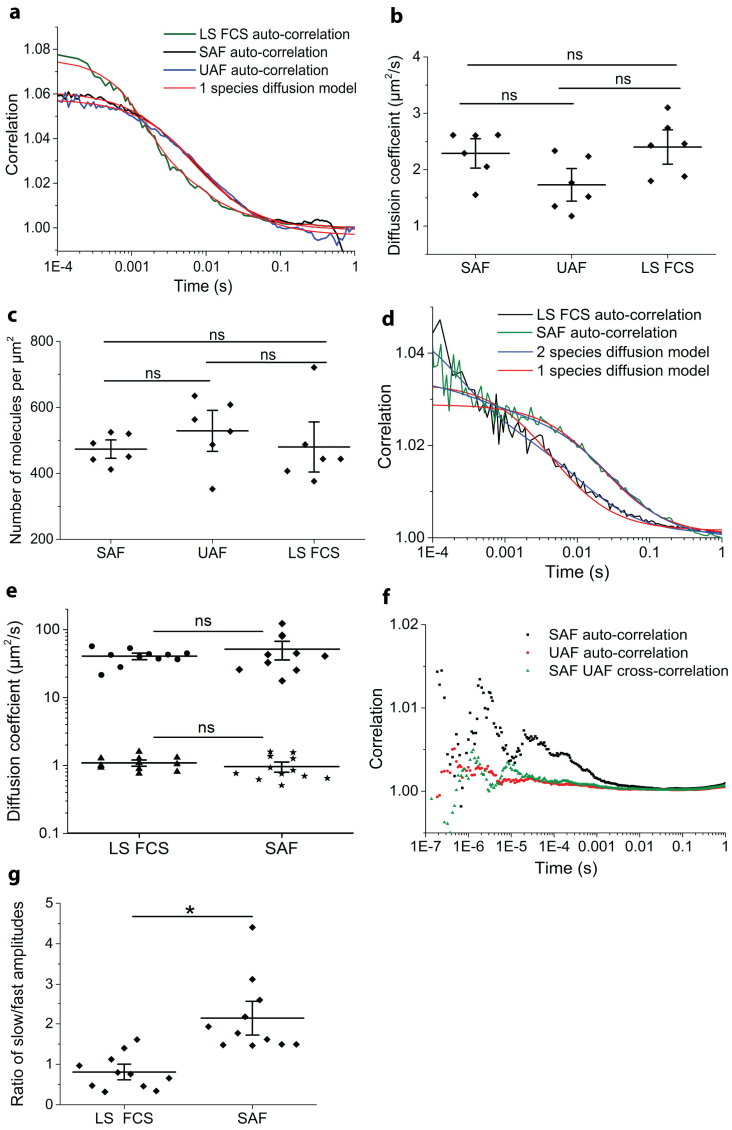

Fig. 3. Comparison of LS FCS, SAF FCS and UAF FCS measurements of model and cell membranes. (**a**) Autocorrelation curves obtained by LS FCS (green), SAF FCS (black) and UAF FCS (blue) of DHPE-OG488 (20 nM) in supported lipid bilayers. The data was fitted to a one-species two-dimensional free diffusion model (red lines). (**b, c**) Diffusion coefficients (**b**) and concentrations (**c**) obtained from LS FCS, SAF FCS and UAF FCS measurements of DHPE-OG488 in lipid bilayers. Each symbol represents an independent experiment (n = 6), horizontal and vertical bars represent means and standard errors (*P<0.05, two-tailed t-test). (**d**) Fitting of the LS FCS auto-correlation curve (black line) of Lck10-EGFP in COS-7 cells to one-species (red line) and two-species (blue line) two-dimensional diffusion models. (**e, g**) Diffusion coefficients (e), and ratio of amplitudes (g) of the slow and fast diffusion components (P = 0.35 and 0.31 for the slow and fast Lck10-EGFP components, respectively) of Lck10-EGFP obtained by LS FCS and SAF FCS. Values were extracted by fitting autocorrelation curves to two-species diffusion model, yielding diffusion coefficients for slow (triangle and stars) and fast (circle and diamond) diffusion components for both LS FCS and SAF FCS measurements. Each symbol represents an independent experiment (n = 11), horizontal and vertical bars represent means and standard errors (*P = 0.012 in **g**). (**f**) SAF FCS, UAF FCS and cross-correlation of SAF and UAF of free diffusing cytosolic EGFP in COS-7 cells. Data shown in **f** is representative of 6 measurements.

#255838 Received 21 Dec 2015; revised 16 Mar 2016; accepted 17 Mar 2016; published 29 Mar 2016

A fitting-free method can be employed to yield an efficient measure of the average fluctuation behavior within a population of interest (Fig. 4(a)). This approach uses the half correlation time $T_{1/2}$ to give the effective diffusion time of particles within the detection volume regardless the underline diffusion mode, which can then yield the corresponding diffusion coefficient using Eq. (4) [18]. We extracted a diffusion coefficient of Lck10-EGFP from the SAF FCS data as 1.60 ± 0.73 $\mu m^2/s$ which was statistical significantly slower than the LS FCS value of 2.76 ± 1.33 $\mu m^2/s$ (n = 10, **P* = 0.039 (Fig. 4(b)). The number of molecules per area measured by the two methods was similar (Fig. 4(c)). This result confirmed the notion that the diffusion of membrane FCS measurement by confocal setup can be biased by the fluctuation of cytosolic fractions of the molecules.

Together these data demonstrates that proteins with the Lck membrane anchor have both a membrane-associated and cytosolic fraction in cells. This makes it highly likely that the full-length Lck protein is also distributed between the plasma membrane and the cytoplasm.

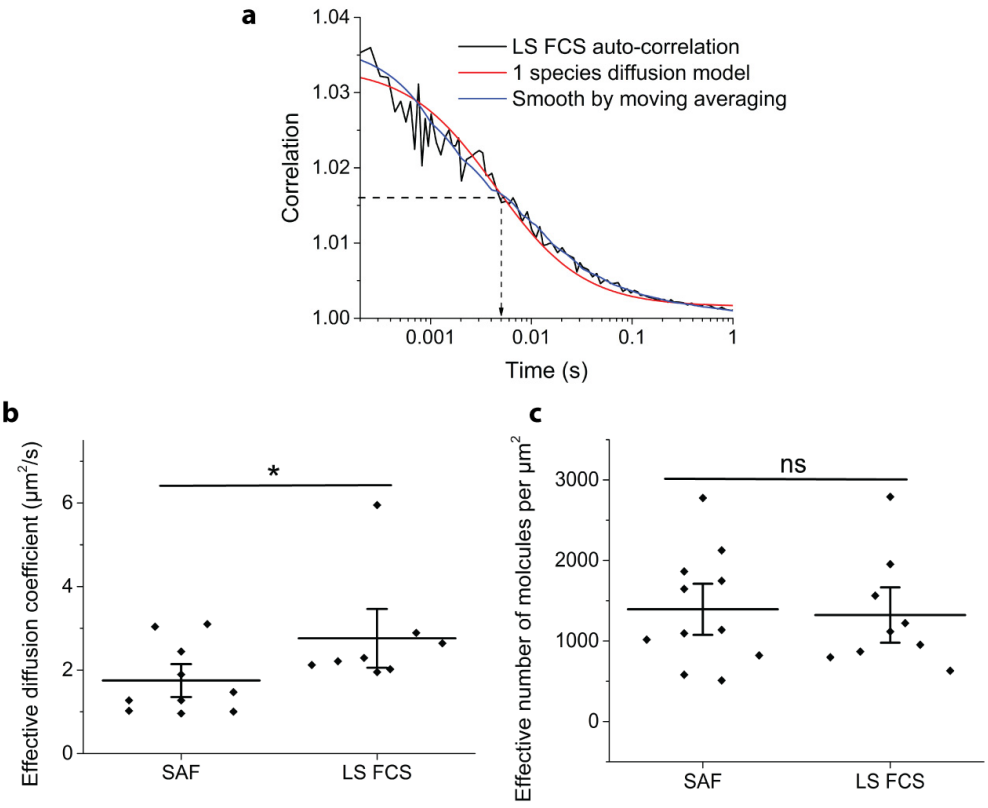

Fig. 4. Analysis of auto-correlation curves by the fitting-free $T_{1/2}$ method. (**a**) Reprehensive example of analysis of Lck10-EGFP diffusion time by diffusion model fitting or $T_{1/2}$ method, see Methods. This $T_{1/2}$ value is indicated by dotted lines in the graph. The amplitude of the correlation curve is defined as the G(γ) value at 200 μs. (**b, c**) Plot of diffusion coefficient (b) and concentration (c) of Lck10 EGFP in COS-7 cells by SAF and LS FCS by the $T_{1/2}$ method. The mean (black solid line) and standard error bar are indicated (n = 10, **P* = 0.039 and 0.60 in b and c, respectively).

3.3. Diffusion and membrane association of full-length Lck during T cell activation

Jurkat cells were transiently transfected with Lck-EGFP and placed on non-activating surfaces (glass coverslips coated with anti-CD90 antibodies), or on activating surfaces (glass coverslip coated by anti-CD3 and anti-CD28 antibodies). For both conditions, the auto-correlation curves of Lck-EGFP in the SAF channel were recorded for the membranes

#255838 Received 21 Dec 2015; revised 16 Mar 2016; accepted 17 Mar 2016; published 29 Mar 2016

adjacent to the glass surfaces. As above, the autocorrelation curve fit best to a two-species model compared to a one-species model (Fig. 5(a)). We extracted values for the diffusion coefficients of 0.49 ± 0.44 $\mu m^2/s$ and 36.7 ± 36.3 $\mu m^2/s$ for membrane-associated and cytosolic Lck-EFGP, respectively, in resting T cells, and 0.58 ± 0.38$\mu m^2/s$ and 51.94 ± 25.05 $\mu m^2/s$ for membrane-associated and cytosolic Lck-EGFP, respectively, in activated T cells. The values for membrane-associated Lck agree well with published data [15, 16, 25].

There was no statistical difference in diffusion coefficient between the resting and activated conditions for both the membrane-associated and cytosolic species (Fig. 5(b)). However, a significant increase in the ratio of amplitude between membrane and cytosolic Lck in the activated condition was observed (Fig. 5(c)). At the same time a difference in the effective diffusion coefficient of Lck in resting and activated condition was observed by the $T_{1/2}$ analysis (Fig. 5(d)), where the diffusion constant was decreased from 3.73 ± 1.79 $\mu m^2/s$ in the resting state to 2.55 ± 1.04 $\mu m^2/s$ under activated conditions. We reasoned this decrease could be due to the increased weighting of the membrane Lck fluctuations under activated conditions. Molecular brightness analysis shows that this enhancement in the membrane-bound contribution is not due to an increase in brightness of the membrane-bound Lck-EGFP fraction, nor is this increase due to a change in concentration of membrane-bound Lck-EGFP (Fig. 5(e)). Two remaining hypotheses for this behavior are an increase in concentration of membrane-adjacent cytosolic Lck-EGFP (as opposed to freely diffusing cytosolic Lck-EGFP) or by a decrease in molecular brightness of this sub-population of cytosolic particles due to an increase in their distance from the coverslip surface. As the membrane-bound fraction does not show a change in molecular brightness under activating versus resting conditions (data not shown) it suggests that there is no large motion of the cell membrane itself, suggesting that the distance between the cytosolic side of the membrane and the coverslip surface is constant. As a consequence, the increase in membrane-bound Lck-EGFP contribution to the observed fluctuation signal is attributed to an increase in cytosolic Lck-EGFP immediately adjacent to the cell membrane.

#255838 Received 21 Dec 2015; revised 16 Mar 2016; accepted 17 Mar 2016; published 29 Mar 2016

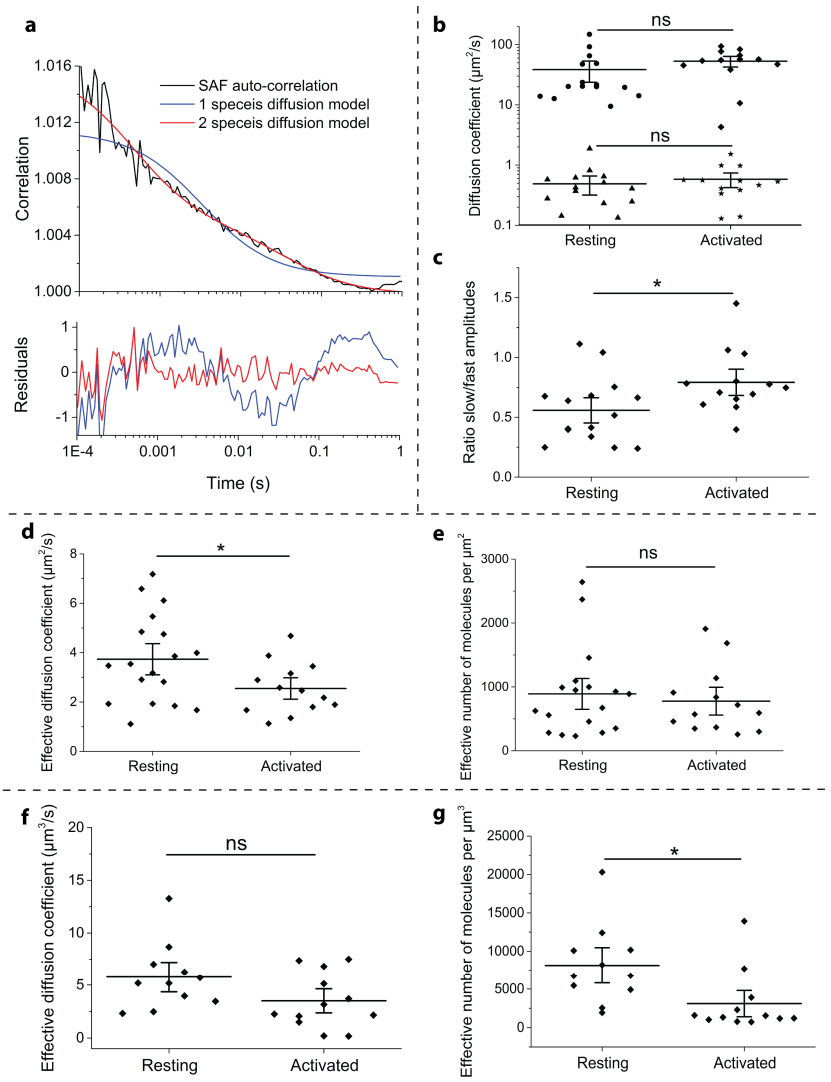

Fig. 5. Diffusion analysis of Lck in resting and activated T cells with SAF FCS. (**a**) Auto-correlation curve (black line) of Lck-EGFP in activated T cells fitted to a one-species two-dimensional diffusion model (blue line) and two-species two-dimensional (red line) diffusion model. The fitting residuals are plotted below. (**b, c**) Diffusion coefficients (b) and the ratio of amplitudes of the slow to fast components (c) of Lck-EGFP in resting and activated Jurkat cells obtained by fitting SAF FCS data to two-species diffusion model, resulting in values for slow (triangle and stars) and fast (circle and diamond) diffusing Lck-EGFP species. Each symbol represents an independent experiment (n = 15), horizontal and vertical bars represent means and standard errors (P = 0.56 and 0.25 for the slow and fast Lck-EGFP components, respectively in b, *P = 0.030 in c, two-tailed t-test). (**d, e**) Average diffusion coefficient (d) and average concentrations (e) of Lck-GFP extracted by the $T_{1/2}$ method of the data sets shown in (b). ns, not significant; *P = 0.04 in (d) and P = 0.62 in (e). (**f, g**) Average diffusion coefficient (f) and average concentrations (g) of Lck-EGFP extracted by the $T_{1/2}$ method for the signal collected in the UAF channel. Each symbol represents an independent experiment (n = 11), horizontal and vertical bars means and standard errors (P = 0.07 in f and *P = 0.015 in g).

If this translocation of cytosolic Lck to the membrane-adjacent region is in fact the underlying behavior, a corresponding drop in freely-diffusion cytosolic Lck would also be expected. This cytosolic signal is conveniently available in the UAF channel

#255838 Received 21 Dec 2015; revised 16 Mar 2016; accepted 17 Mar 2016; published 29 Mar 2016

contemporaneously with the SAF signal. The low amplitude fluctuations observed in the corresponding UAF channel were insufficient to yield effective autocorrelation curves for direct fitting, the more robust fitting-free $T_{1/2}$ method could still be applied. The results suggest that there was no significant change of diffusion dynamics of Lck-EGFP in the UAF channel (Fig. 5(f)). Interestingly, a nearly 3-fold reduction of Lck-EGFP concentration was observed in activated T cells (Fig. 5(g)). Giving that the fluctuations in the UAF channel were mainly determined by the freely-diffusing cytosolic fraction, the data indicates that the concentration of cytosolic Lck-EGFP was reduced upon T cell activation. This observation confirms the hypothesis that together, it can thus be concluded that Lck translocates from the cytoplasm to the plasma membrane-adjacent region upon T cell activation.

4. Conclusion

The lateral and axial confinement of the detection volume with a SAF objective makes the setup ideal for FCS analysis of biological membranes. Previous studies have demonstrated the proof-of-principle for SAF FCS [6, 8] using custom-built microscopes. Here, we demonstrated that SAF objective could be incorporated into a commercial microscope with relative simple modifications to the light path.

By performing a range of FCS measurements on supported lipid bilayers, we characterized and demonstrated that the SAF objective was an excellent choice for membrane FCS measurement. Our data highlighted one of the drawbacks of confocal FCS method for membrane measurement and how SAF FCS overcomes that issue, that is the 'contamination' by fast moving cytosolic molecules in lateral diffusion measurements, which can dominate the signals from the membrane molecules [8]. The detection volume in our SAF setup was an order of magnitude smaller than in conventional confocal FCS due to this exceptional axial confinement even with a lower NA than can be achieved with confocal FCS.

These benefits were clearly demonstrated by diffusion and concentration analysis of Lck10-EGFP in COS-7 cells by SAF FCS and LS FCS, where SAF successfully rejected the cytosolic signals and produced more reliable results than confocal FCS. Employing SAF FCS, we measured that the diffusion and concentration of Lck in resting and activated T cells. The result showed slower diffusion of Lck in activated T cells, which is consistent with previous studies that suggest Lck becomes immobilized at the site of TCR triggering [15, 25]. The concentration analysis with both SAF and UAF FCS suggested a translocation of Lck molecules from the cytoplasm to the plasma membrane during T cell activation, which is also in agreement with previously reported TIRF data [16]. More generally, our results highlight that receptor activation could result in the redistribution of proteins between the cytoplasm and membrane as membrane anchors do not necessarily stably associate proteins with the plasma membrane.

In summary, we demonstrated in the current study that a SAF objective is an excellent choice for membrane FCS measurements. With its effective z-discrimination, SAF is insensitive to fluorophores not immediately above the coverslip surface, which can lead to problems in conventional confocal-based FCS measurement. Importantly, we showed that SAF could be easily adapted to existing commercial microscopes that simultaneously captured UAF so that information from fluorophores away from the coverslip could simultaneously be captured. These instrumental advantages make this approach optimal for studying membrane dynamics and we foresee a widespread use of SAF for these investigations in the future.

Acknowledgments

We thank the Australian Research Council and National Health and Medical Research Council of Australia (APP1037320, APP1059278 and APP1022182) for funding this project. We would also like to thank the staffs at Bio Medical Imaging Facility at University of New South Wales for their technical advices.

#255838 Received 21 Dec 2015; revised 16 Mar 2016; accepted 17 Mar 2016; published 29 Mar 2016